Physics of Plasmas

Interpreting ion-energy distributions using charge exchange emitted from deeply kinetic field-reversed-configuration plasmas

Cite as: Phys. Plasmas **29**, 052508 (2022); https://doi.org/10.1063/5.0089430
Submitted: 25 February 2022 • Accepted: 01 May 2022 • Published Online: 19 May 2022

A. H. Glasser and S. A. Cohen

Physics of Plasmas ARTICLE scitation.org/journal/php

Interpreting ion-energy distributions using charge exchange emitted from deeply kinetic field-reversed-configuration plasmas

Cite as: Phys. Plasmas **29**, 052508 (2022); doi: 10.1063/5.0089430
Submitted: 25 February 2022 · Accepted: 1 May 2022 ·
Published Online: 19 May 2022

A. H. Glasser[1,a] and S. A. Cohen[2,b]

AFFILIATIONS

[1]Fusion Theory and Computation, Inc., 24062 Seatter Lane NE, Kingston, Washington 98346, USA
[2]Princeton Plasma Physics Laboratory, P.O. Box 451, Princeton, New Jersey 08543, USA

[a)]aglasser5@gmail.com
[b)]Author to whom correspondence should be addressed: scohen@pppl.gov

ABSTRACT

Energy resolving the atomic hydrogen outflux created within plasmas by charge exchange (CX) of hot plasma ions with cooler hydrogen neutrals is used to infer the ion energy distribution within the plasma, IED_p. In high-β plasma with field nulls and ion gyro-radii comparable to the plasma size, the measured ion energy distribution (IED_m) of the CX outflux will depend on the viewing angle and position of the detector. We describe the physics for this, results from a synthetic diagnostic code that contrasts the IED_m to the IED_p within relatively small and hot field-reversed-configuration plasmas, and how these data can show the presence of magnetic nulls and different orbit classes in the plasma.

I. INTRODUCTION

Knowing the ion energy distribution (IED_p) is important for many plasmas, all the more so for fusion plasmas where the reaction rate is a strong function of ion energy, and instabilities may be triggered and/or driven by non-Maxwellian ion energy distributions. Low atomic number (Z) fuel ions in hot fusion plasmas are fully ionized, making common spectral methods, such as line shift or broadening, difficult. Line radiation emitted by higher Z elements—whether naturally occurring or purposely introduced into the plasma—is often used as a proxy. However, questions arise, then concerning the similarity of the respective energy distributions or even whether thermal equilibrium exists between the impurity and the fuel ions.[1]

Particle methods are alternatives for measuring the IED_p. In fusion research, the charge-exchange (CX) stripping-cell ion-energy analyzer (SC-IEA) is a gold-standard technique.[2] It, too, has limitations such as opacity to neutrals. For small, low-density plasmas as considered here, opacity is a minor concern. SC-IEAs applied to measure the IED_p in moderate-scale tokamaks[3] ordinarily view radially, toward the minor axis. Shifting an SC-IEA's line-of-sight (LOS) from the minor axis can provide the line-integral of the IED_p's radial dependence because the ion motion is predominantly cyclotron with ion gyro-radii small compared to the plasma radius. This condition is satisfied low-β tokamaks. If energetic neutral beams are injected tangentially, SC-IEAs should also look along and against the beam direction.

In this paper, we consider how this situation differs in small, high-β, magnetic fusion energy (MFE) research facilities, focusing on RF-heated, low-s, field-reversed-configuration (FRC) devices, where[4]

$$s \sim 0.3 r_s/{}_M\rho_i. \tag{1}$$

Here, r_s is the separatrix radius at the midplane, ${}_M\rho_i$ is the ion gyro-radius at the maximum magnetic field, at $r = 0$ in the midplane, $z = 0$, and z is the major axis, see Fig. 1. The difference arises because other classes of orbits exist in FRCs, not only the cyclotron. This, along with the heating method and low ratios of the heating and confinement times to the thermal equilibration time, causes the IED_p to be kinetic, not Maxwellian.

In Sec. II, we review the classes of orbits and their locations within FRCs, explaining why the LOS of the SC-IEA is so important for determining the plasma's IED_p. Section III describes the synthetic diagnostic (SD) numerical module within the single-particle RMF code used to predict the energy-resolved CX outflux. Section IV presents results of particle-trajectory simulations for a currently

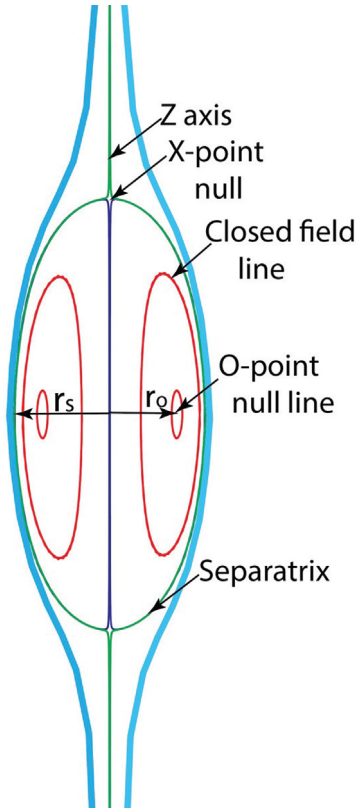

FIG. 1. Schematic of a prolate FRC's field lines in an r–z plane. Magnetic field nulls, the FRC's separatrix radius, r_s, and O-point radius, r_o, at z = 0 are labeled.

operating RF-heated FRC and the energy-resolved CX outflux predicted by the SD module *vs* the IED_p in the plasma. Section V discusses and summarizes the results and provides conclusions.

II. ORBIT CLASSES AND LOCATIONS IN FRCS

An FRC[5] is a magnetized plasma of toroidal shape, often prolate and usually with no hole along the major axis, see Fig. 1. The toroidal shape is a result of an azimuthal current ring in the plasma, which is inside a coaxial quasi-solenoidal magnet array. The magnetic field has an O-point null line at $r = r_o$ on the $z = 0$ midplane. The plasma current is parallel to the O-point null line. The field has spindle X-point nulls, one at each end, at $z = \pm z_s = \pm \kappa r_s$, with κ the elongation.

An FRC has no toroidal magnetic field; field lines do not circulate toroidally (azimuthally). All magnetic field lines inside a separatrix, $r = r_s$ on the midplane, close on themselves after one poloidal circuit, hence do not form closed magnetic surfaces but simple loops (red in Fig. 1), each approximately on an *r*-*z* plane. The separatrix is the boundary between the closed field-line region and the open field-line region.

The great majority of cool charged particles in FRCs do not move toroidally at their thermal speed but slowly ∇B and curve-B drift with the sign of that slow motion matching that of their canonical azimuthal (ϕ) momentum, π_ϕ. The trajectories of particles crossing the null line will reverse their sign of curvature. These particles' orbits fall into two new classes, betatron and figure-8, see Fig. 2.[6,7]

These new orbit classes are generally more energetic than cyclotron orbits, hence have larger curvature and smaller *s*. All betatron-orbit ions freely circulate at near their thermal speed in the opposite azimuthal direction as the cyclotron-orbit ions drift. Ion and electron betatron orbits move in opposite azimuthal directions. Depending on the sign of their π_ϕ, the net figure-8 orbital motion may be either CW or CCW. Part of the figure-8 orbital motion, when the orbit is near the null, is always CW. Both betatron and figure-8 orbits pass over the O-point null line. Cyclotron orbits exist either fully inside or fully outside the O-point null line; few (see Fig. 2, cyclotron 2) encircle the major axis at their thermal speed.

Three detector LOS chords/pipes are indicated by the gray rectangles in Fig. 2; detectors placed on the right (left) of the figure receive CW- (CCW-)moving particles created by CX. The y and z dimensions of an LOS are small fractions of the plasma's size. The plasma current is in the CCW direction.

As shown in Fig. 2, with trajectories calculated by the RMF code,[8] the CX outflux from cyclotron orbits will be seen by both the CW-orbit-viewing (CW-OV) and CCW-OV detectors of all three LOS. (For this FRC orientation, a CCW-OV detector looks into the plasma current.) Arrows indicate the instantaneous direction of an ion's motion at positions in the six detectors' LOS.

Figure-8 orbits passing through chords 1 and 2 will be seen only in the CCW-OV detector but by both detectors of chord 3. A detector viewing a chord tangent to (or nearly tangent to) the O-point null line will see few betatron or figure-8 orbits. Betatron orbits will be seen by CCW-OV detectors of chords 1 and 2. For chord 3, only a few

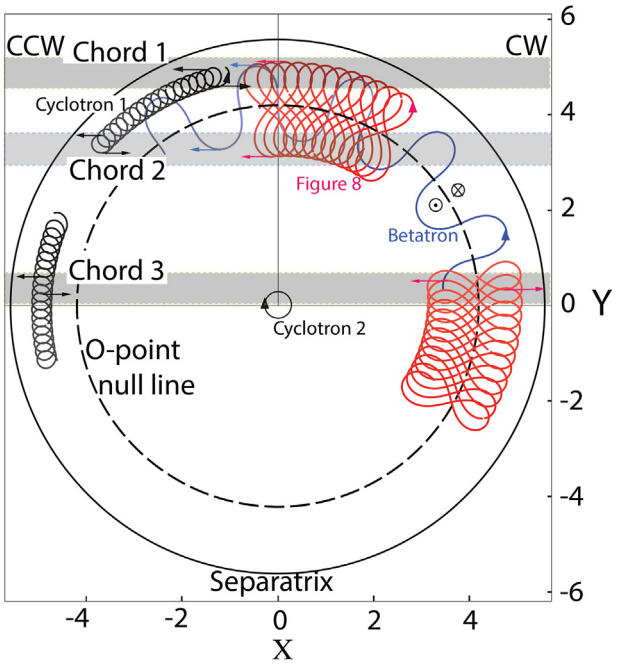

FIG. 2. Trajectories of sample ions in an FRC's z = 0 midplane. Three detector viewing chords are indicated by the gray rectangles. A detector may view orbits moving in either the CCW or CW direction; hence, six detectors view the three chords. B(0, 0) = 1000 G, r_s = 5.5 cm. Arrows indicate the direction of ion motion. All spatial dimensions in this paper are in cm.

betatron orbits—those with velocity nearly perpendicular to the O-point null—will contribute signal to both CCW-OV and CW-OV detectors. High-energy figure-8 orbits may encircle the major axis each time a single figure-8 is performed. Both figure-8 and betatron obits may extend beyond the separatrix.

When a particle is not restricted to the z = 0 invariant subspace, its trajectory may approach the X-point nulls and become chaotic with velocity randomized by collisions with the curve-changing weakening magnetic field. (The Lorentz force pushes cyclotron orbits, and co-moving figure-8 orbits, away from the midplane, but betatron orbits toward it.) During these "collision-less" collisions[9] with the *magnetic field* near the x point, the particle's energy remains constant, but μ, the magnetic moment, changes. The orbit shape frequently jumps between figure-8 and cyclotron.

As implied above, detectors viewing different y chords and z positions should allow localization of the X-point position and the O-point and separatrix radii and identification of the orbit classes. For example, all field lines beyond the x point are open. Particle and energy losses there should be high, hence the CX signal and temperature low.

The different particle classes populate different spatial regions of an FRC. The density in each class will depend on the type of plasma heating.

Figure 3 presents results from single-particle simulation of a Hill's vortex FRC with $B(0,0) = 1000$ G, $r_s = 6$ cm, $\kappa = 2$, $B_{RMF} = 40$ G, and $f_{RMF} = 2.7$ MHz. For this simulation, the RMF_o rotates in the ion diamagnetic direction, and τ is measured in units $2\pi/\omega_{ci}$. In "real" time, this simulation was for 0.7 ms, about 14 times the expected ion energy confinement time. The 90° ion–ion pitch-angle scattering time at 100 eV and 10^{13} cm^{-3} is 0.6 ms, and the electron-ion thermalization time is 1.8 ms. During the period $1300 < \tau < 2000$, when the particle was most energetic, it is in a betatron orbit, Fig. 4, and populates the region $|z| < 5$ cm and $2 < r < 9$ cm, see Figs. 5 and 6.[10] Though the ion energy reached 600 eV, the average ion energy was near 100 eV, in large part because of the 0.5 ms ($\tau < 1300$) delay before the ion became energized. Note that the cyclotron orbits

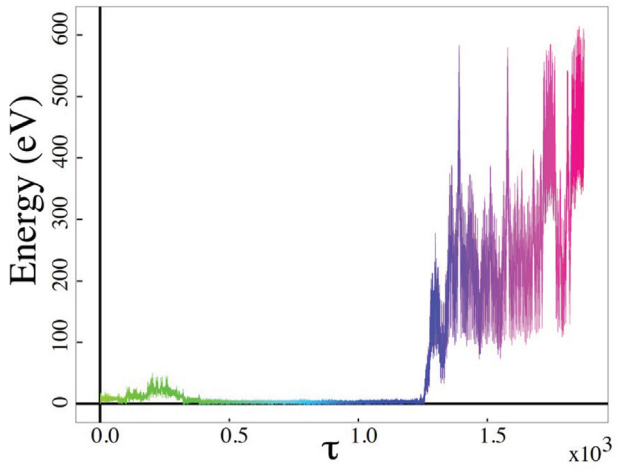

FIG. 3. Energy vs time for H^+ heated by RMF_o at $\omega = 1.8\omega_{ci}$, where ω_{ci} is 2π times the ion cyclotron frequency at B(0, 0). Time is color coded. Explosive heating occurs at $\tau = 1250$ in a time <50 μs.

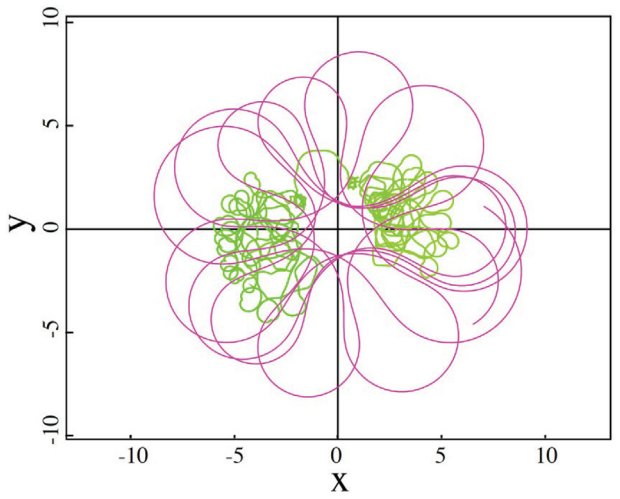

FIG. 4. H^+ orbit shapes, projected on the z = 0 plane, for $\tau \approx 100$ and 1600. The color coding corresponds to that in Fig. 3.

remained inside r_s, while the betatron orbits extended beyond r_s. An ion with an energy of 600 eV has a velocity about 35% of the RMF_o speed at $r = r_o$.

Many more simulations with varied initial parameters, as described in Sec. IV, will guide us to where in the FRC the detector should look to get IED_m from which to extract the most information on the IED_p and the FRC itself.

The current profile in FRCs is often modeled as a rigid rotor (RR).[11] Alternatively, 2D results for both the current and density can be found from the Grad–Shafranov equation,[12] 2D reconstruction of measured equilibria, or PIC,[13] hybrid,[14,15] or MHD[16] codes. One

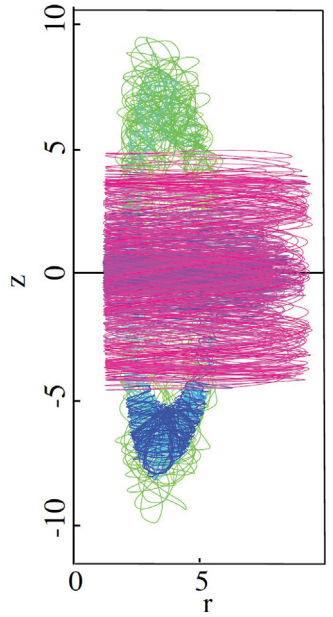

FIG. 5. H^+ trajectory projection onto the r–z plane.

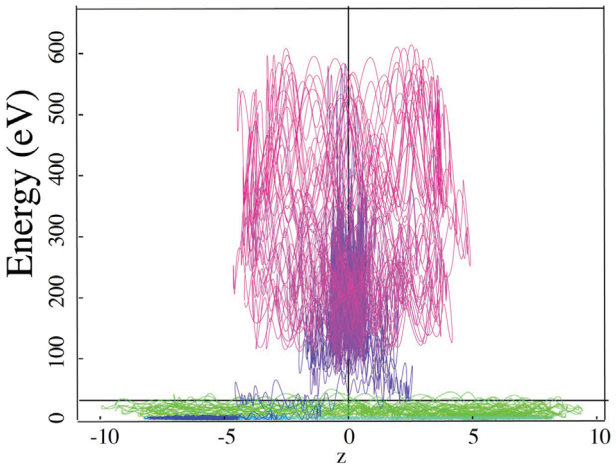

FIG. 6. Ion energy vs z. The more energetic betatron orbits have a lesser axial (z) extent.

common feature of all these models is that the density peaks at the O-point null line and is low both at the separatrix and at the major axis. In addition to pressure balance, the low density near the z axis is due to plasma losses from those field lines to the open field lines, as the field lines proceed poloidally to the separatrix. Some experiments[17] have shown flat profiles rather than hollow ones, hence despite the apparent uniformity of many theoretical predictions, detailed measured density profiles are necessary when estimating IED_p extracted from the SC-IEA data.

III. THE SYNTHETIC DIAGNOSTIC MODULE OF THE RMF CODE

By solving Hamilton's equations for the full orbit, the RMF code calculates the trajectory of an individual charged particle in a specified time and spatially varying magnetic and electric fields. The time step is set by restricting the variation of the Hamiltonian in the RMF_o's rotating frame to selected relative tolerance, typically in the range of 10^{-8}–10^{-12}. The more restrictive tolerance value fixes the time step to correspond to less than 10^{-3} of the shortest gyro-period. The particle's initial position and velocity are input parameters as are the FRC's shape and magnetic field and the *RMF*'s parity, strength, rotation direction, frequency, and axial wavenumber.

The SD module examines the RMF-calculated position and velocity of a particle at each time step. For computational efficiency, the SD module may evaluate several SC-IEA detector axial positions, each with a view tangent to a selected radius. The SD module first checks whether the particle's position places it in a disk of thickness $\pm\Delta z$ corresponding to one of the specified detector axial positions. The SD module then checks whether the particle's velocity vector allows it to reach a detector with a specified solid-angle acceptance. To reduce the required computation time, for each specified z disk, we define an infinite number of detector LOS, covering all azimuthal angles, each in the plane of that disk and tangent to the specified radius. Detectors viewing one disk accept particles moving in either the CW or CCW directions that would escape by CX. At each time step, the SD module records "hits" for a detector and normalizes them to the time spent traversing that location. For each hit—a particle having the correct velocity vector to enter a particular detector—the particle energy is recorded. For each disk and each tangent radius, the data for those detectors are sorted into two groups: CW-OV and CCW-OV.

In the simulations that follow, we assume a flat neutral hydrogen profile in the plasma, as has recently been measured in the Princeton field-reversed configuration-2 (PFRC-2) by the two-photon absorption laser induced fluorescence (TALIF) method.[18]

IV. RESULTS OF SD SIMULATIONS

Prior to presenting SD simulation results for RMF_o-heated Hill's vortex FRC plasmas, we note two points about ion orbits in the mirror configuration. Because there are no magnetic nulls in a magnetic mirror, only cyclotron orbits exist. These fall into two categories, those that encircle the z axis during each gyro-orbit and those which drift slowly around the z axis, encircling it only via their drift motion. Those in the first category could be of four times higher energy than those in the second and would be seen by only one orientation of CX detector, CW or CCW orbit viewing, depending on the direction of the axial magnetic field (or the plasma current). Because a mirror field's strength varies little in the radial direction, an axis encircling ion needs high energy to reach the outer periphery of the plasma, about six times greater than a betatron orbit and 30 times greater than a figure-8 orbit in an FRC having the same radial size and same on-axis central magnetic field strength. Concerning the axial dependence of the ion orbits, the increase in magnetic field strength toward the mirror throat increases both the ion density and its perpendicular energy in the single-particle picture.

One important reason for choosing a Hill's vortex comparable in size to the PFRC-2 to model is to provide an existing and appropriate experiment a means to interpret its IED_m SC-IEA data. As shown in Figs. 4–6, RMF_o is expected to preferentially energize particles near the axial midplane in the direction perpendicular to the FRC's magnetic field there. SC-IEA data could test this prediction. Additionally, the SC-IEA spectrum shape could inform studies of plasma fluctuations that might cause transport and thermalization, phenomena not included in RMF-code modeling. An exponentially decaying spectrum, with no truncation, is a sign of thermalization. Equally important is to show the utility of the SC-IEA to reveal whether magnetic nulls appear in the plasma.

The expected ranges of PFRC-2 plasma parameters are $T_e = 400\pm200$ eV, $\bar{E}_{H^+} = 150\pm100$ eV, $B(0,0) = 1100\pm300$ G, $r_s = 5\pm1$ cm, $\kappa = 1.5\pm0.5$, $n_e = 1$–3×10^{13} cm^{-3}, $\langle\beta\rangle$ to 0.8, and B_{RMF_o} to 50 G. At an absorbed RMF_o power of 100 kW and the above parameters, the energy confinement time, τ_E, is of order 50 μs. In the RMF code, the plasma density and temperature are not specified. The RMF_o frequency can be changed in the RMF code for each simulation.

The plasma density (n_e) and H^o and H_2 densities were measured in the PFRC-2 at about 1/3 of the target vacuum field strength and RMF_o power and found to be near 5×10^{12}, 10^{11}, and 10^{12} cm^{-3}, respectively; the H_o density[18] was constant across the cross section, consistent with the mean-free path of Franck–Condon neutrals formed by H_2 dissociation.

To date, the PFRC-2 has operated at an RMF_o frequency between 4 and 14 MHz. Lowering the RMF_o frequency to 2 MHz is in progress. For most simulations, we assumed a frequency close to 2 MHz, which is expected—as soon to be shown—to give good ion heating at

achievable magnetic fields. The PFRC-2's maximum midplane central vacuum magnetic field, $B(0, 0)$, is 850 G.

As an FRC forms in the PFRC-2, field compression against the 16-cm-ID internal superconducting flux-conserving coaxial rings can increase B(0, 0) to about 3500 G, which would occur when the separatrix radius reached 7 cm and the initial vacuum field was 850 G. For this case, the ratio of the RMF_o frequency to the ion cyclotron frequency, $\Omega \equiv \omega_{RMF}/\omega_{ci}$, would be -0.4. (The appropriate sign of Ω is negative because the RMF_o rotates in the electron betatron direction in order for there to be RMF penetration into the plasma and efficient electron current drive. Efforts are now being made to develop an RF heating system, which will simultaneously provide positive Ω for better ion heating in FRCs, as shown in Sec. IV A.)

For the simulations reported here, we have restricted attention to less challenging values of the magnetic field, obtained by assuming a lower vacuum magnetic field and less field compression against the flux conservers. Simulations at higher magnetic field show higher ion energies.

A. Ion energy distribution within the plasma

RMF-code studies with the SD module were made with variations over the aforementioned ranges of r_s, $B(0, 0)$, B_{RMF}, κ, and Ω, along with variations of the initial energy and position of the ions: $0.02 < E_i < 5$ eV, $0 < r_i/r_s < 1.1$, and $0 < z_i/z_s < 0.8$, and angles of the initial particle velocity and RMF_o phase, where subscript i refers to the initial value.

The energy and confinement of ions depends strongly on Ω and B_{RMF} and less strongly on initial position. Figure 7 shows the Ω dependence of the maximum energy and Fig. 8 the inverse of the particle loss time, τ_{max}, from 1800 simulations of maximum duration $\tau = 5000$. τ_{max} is defined as when the particle position exceeds 1.1x of the flux conserver internal radius or 1.1x the X-point position. More heating occurs for $-1.2 < \Omega < -0.4$ and higher B_{RMF}, though accompanied by more rapid ion loss. We apply the term "heating"

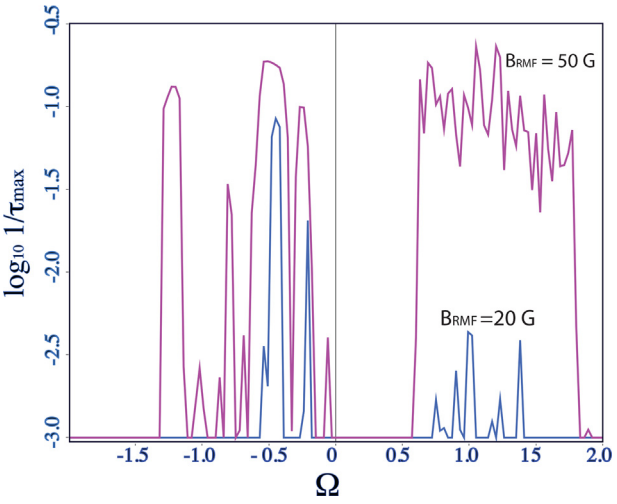

FIG. 8. Log $(1/\tau_{max})$ vs Ω.

when the IED_p has a decaying exponential shape, though truncated at high energy. Heating corresponds to stochastic orbits, with positive Lyapunov eigenvalues. For $B_{RMF} = 50$ G, a "sweet" spot, excellent heating and low losses, is seen near $\Omega = -1$. For lower RMF_o power, corresponding to lower B_{RMF}, the sweet spot is at smaller $|\Omega|$. Changing the initial position of the particle can also change the maximum energy achieved.

Figure 9 displays the difference between a quasi-thermalized IED_p, as obtained when $\Omega = -1.05$, and a periodically energized/de-energized ion, when $\Omega = -2$.

The former lies in the "noisy" region and the latter in the smooth region, as shown in Figs. 7 and 8, respectively. Both are truncated distributions. At $\Omega = -2$, the distribution is cut off at lower energy, *ca.*, 90 eV, and is cup shaped. The particle does not reach higher energy

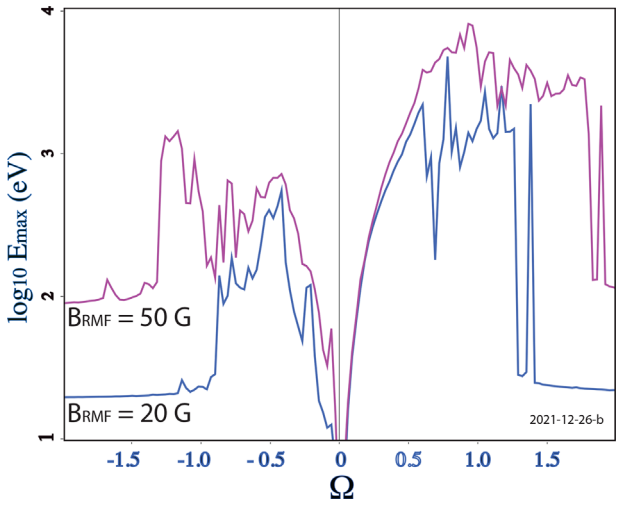

FIG. 7. Maximum H^+ energy within the FRC for two different RMF_o field strengths, 20 and 50 G vs Ω. $r_s = 5.7$ cm, $\kappa = 1.5$, and B(0, 0) = 1200 G. The ion's initial energy was 2 eV and the initial position was r = 4.9 cm and z = 2.2 cm.

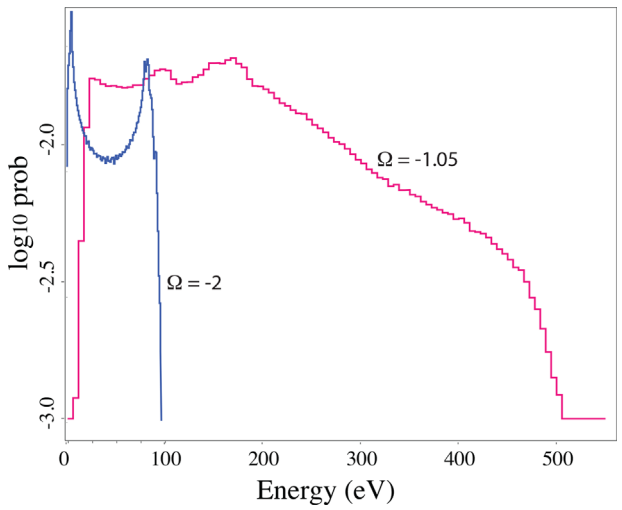

FIG. 9. Log IED_p vs energy for $\Omega = -2$ and -1.05. $B_{RMF} = 50$ G, $r_s = 5.7$ cm, $\kappa = 1.5$, and B(0, 0) = 1200 G.

because the threshold for heating is not exceeded. The IED_p at $\Omega = -1.05$ has an exponential shape in the energy range $150 < E < 450$ eV, in part the result of Speiser collisions near the X-points and in part when orbits pass near the O-point null. From the slope of the IED_p in the energy range $150 < E < 450$ eV, the effective temperature is 150 eV. This behavior explains why having the PFRC-2 operate in the Ω range between -1.4 and -0.2 is a goal.

IED_ps for two RMF_o field strengths and $\Omega = -1$, within the sweet spot, are shown in Fig. 10. For both, the RMF code predicts truncated exponential distributions with maximum perpendicular energy from Faraday's equation, $\rightarrow W_\perp \sim \pi r_s^2 \omega_{RMF} B_{RMF}$. The parallel energy could increase a similar amount due to the z-parallel electric field created by the z-axis-parallel arms of the RMF_o antennae. The maximum energy increases with the RMF field strength until the loss time becomes too short due to large axial or radial excursions. Loss is then prompt, in a time comparable to the RMF_o period. The ion orbit does not traverse the region of the FRC where the RMF_o-generated electric field is high and B small. Over limited energy ranges, both IED_ps display exponential shapes with similar slope. The main difference is the location of the truncation.

B. SC-IEA-measured ion energy distribution, IED_m

Figures 11 and 12 show IED_ms predicted by the SD module for an FRC with $B(0,0) = 1200$ G, $\Omega = -1.1$, $B_{RMF} = 50$ G, $r_s = 5.7$ cm, and $\kappa = 1.6$. The IED_p is similar to the 40 G case in Fig. 10, though slightly warmer. The IED_ms are for CW-OV and CCW-OV detectors at z = 0 and three tangent radii (elevations), y = 0, 3, and 4 cm above the FRC's z axis. That is, in total, there are six detectors. At the target plasma parameters of ion heating experiments in the PFRC-2, $n_e \sim 10^{13}$ cm^{-3}, $T_e \sim 100$ eV, $\bar{E} \sim 100$ eV, and a H^o density of 10^{10} cm^{-3}, the expected CX neutral outflux is $\sim 10^{14}/($ cm^3 sr s).

Compared to the CCW-OV detector, the CW-OV detector shows both decreased flux and lower temperature at larger tangent radii. The fall-offs in effective temperature and maximum energy as tangent radius increases are striking, about by a factor of 8, clearly inconsistent with the Faraday law estimation but in agreement with our understanding based on orbit classes. The CCW-OV detector shows nearly constant effective temperatures, though the y = 0 detector truncation occurs at 600 eV, while that of the y = 3 and 4 cm is at about 800 eV.

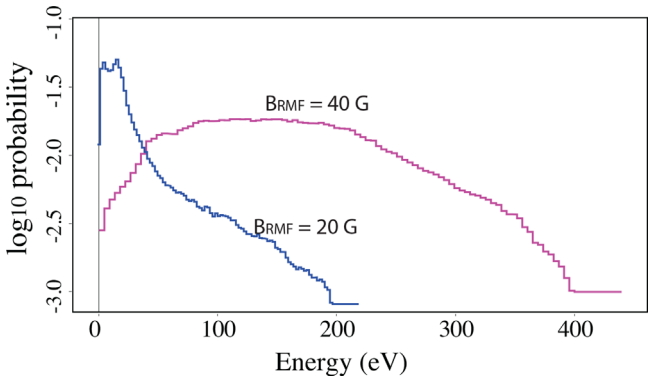

FIG. 10. Ion energy distribution in the plasma, IED_p, for two RMF_o field strengths: $B(0,0) = 1200$ G, $\Omega = -1$, and $r_s = 5.7$ cm.

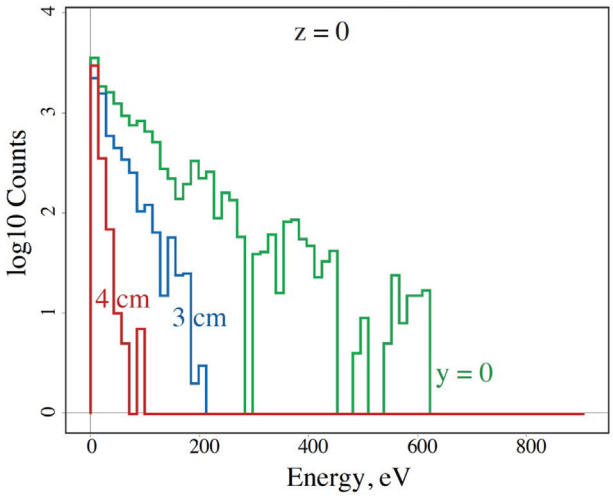

FIG. 11. Ion energy distribution seen by three CW-OV detectors located at z = 0 and detector LOS tangent to three radii, y = 0, 3, and 4 cm.

Figure 13 presents SD predictions on the total energetic CX flux as functions of both z and y detector positions. Data are presented for seven z locations—0, 1.875, 3.75, …, 11.25 cm—of CW-OV and CCW-OV detectors, each with 10 y positions. At each y, z location, the CCW-OV shows a brighter signal. The ratio of CCW-OV to CW-OV brightnesses increases at larger y values, to infinity for $y = 7$–10 cm, i.e., outside the separatrix radius and larger z values. Beyond z = 7.5 cm, where the separatrix is at $y = 3.2$ cm, even the CCW-OV signal has vanished. The maximum energy (not shown) also decreases as z increases beyond 5 cm.

V. DISCUSSION

Using a single-particle Hamiltonian code, we have studied the CX outflux spectrum and amplitude from small, moderate density and

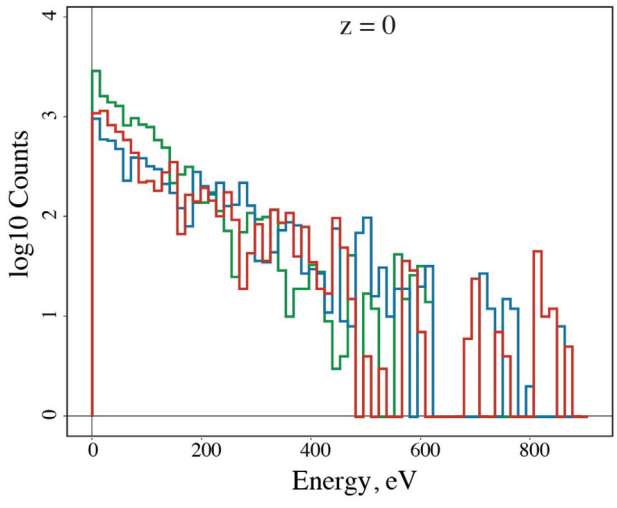

FIG. 12. Ion energy distribution seen by the CCW-OV detector, for detector LOS tangent to three radii, 0, 3, and 4 cm.

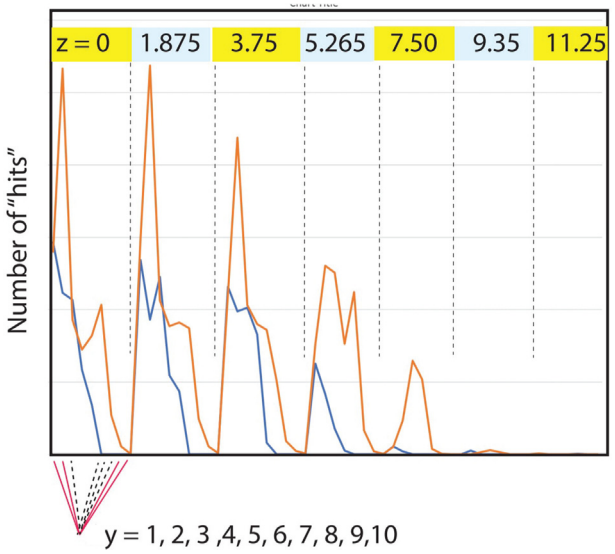

FIG. 13. IED_m for both CW- and CCW-OV detectors for seven z detector positions and ten y positions. (dimensions in cm.) The width of each detector's LOS was ±0.5 cm. Red is for the CCW-OV detectors and blue for the CW-OV detectors.

high-β plasmas with internal magnetic nulls. The plasma model on which we focused attention is a Hill's vortex FRC, with external boundary conditions chosen to avoid a negative plasma pressure outside the separatrix. For two reasons, a Hill's vortex does not accurately represent PFRC-2 plasma: (1) the specific analytic boundary conditions for the Hill's vortex create a magnetic field outside the separatrix that, unlike the PFRC-2, has a large radial component near the X-point; and (2) the PFRC-2's axial magnetic field has an extended region near the midplane where it is straight rather than elliptical. Nevertheless, a Hill's vortex model is attractive because of its mathematical tractability and its representation of generic FRC features, zero toroidal magnetic field, two X-point field nulls, and an O-point field null line.

These studies have shown that the CX outflux is azimuthally asymmetric in both of its amplitude and energy distribution. The charge exchange flux and energy decrease as the viewing position moves closer to the x points. An associated loss of ion-carried current will occur, particularly important when the ion pressure exceeds that of the electrons', as in a reactor.

Because of its strong dependence on the axial and elevation positions of a CX detector and on whether the detector looks parallel to or anti-parallel to the plasma current, this asymmetry will alter interpretation of the measured CX outflux. The viewing into the current anti-parallel direction will show a considerably lower CX temperature and CX outflux amplitude than the into the parallel direction. This difference becomes more prominent at increasing elevations—detector LOS tangency radii—above the axial midplane.

The complexity of the situation, including the shape of the magnetic field, suggests applying machine learning to RMF-code simulations. These would generate a library of spectra for different FRC sizes and shapes and ion heating assumptions. Then, the IED_m at each spatial location could be compared to the library, to conclude what is the IED_p. For this to be accurate, many SC-IEAs would need to be placed on the PFRC.

Measurements on mirror machine plasma, as would occur if the RMF_o power did not form an FRC in the PFRC-2, would yield quite different results. In mirror machines, both the CX signal strength and its (perpendicular) energy would increase moving (axially) away from the midplane because the magnetic field smoothly strengthens and μ is conserved. In contrast, beyond the X-point null in FRCs, in combination with the specifics of the RF heating method, the open field lines (outside the separatrix) and the Lorentz force on the betatron orbits jointly conspire to reduce the signal and average energy of the CX flux as the detector position approaches the X-point and moves beyond it. Additionally, ion heating in a mirror near the midplane would be by a true resonance at $\Omega = -1$. Concerning near-midplane observations, larger energy orbits can be contained in mirror machines because of the near uniform magnetic field across the mirror's radius. For mirror and FRC plasma with the same edge field and plasma radius at the midplane, the maximum energy of an ion whose orbit fits in the plasma is nearly 10 times greater in the mirror than in the FRC.

An important feature of the near-midplane CX outflux parallel to the plasma current will be its extension beyond the separatrix radius. Combined with the high observed energy, this observation will indicate the presence of figure-8 and betatron orbits, signatures of the presence of a null line in the plasma. The location of the reduced CX outflux when viewing against the plasma current will define the separatrix location, within an ion or electron gyro-radius, depending on the ratio of ion cyclotron frequency to ion plasma frequency. For PFRC-2 parameters, the ion gyro-radius will exceed 0.01 m, according to the magnetic sheath theory. The effect of this sheath on the radial excursion of hot figure-8 and betatron orbits needs detailed exploration.

ACKNOWLEDGMENTS

We thank the referees for their thoughtful comments. This work was supported by the U.S. Department of Energy, Office of Science, Office of Fusion Energy under Contract No. DE-AC02-09CH11466.

AUTHOR DECLARATIONS

Conflict of Interest

The authors have no conflicts to disclose.

DATA AVAILABILITY

The data that support the findings of this study are openly available in referenced website at https://dataspace.princeton.edu/handle/88435/dsp01x920g025r, Ref. 19.

REFERENCES

[1]S. Houshmandyar, X. Yang, and R. Magee, "High resolution ion doppler spectroscopy at Prairie View Rotamak," Rev. Sci. Instrum. **83**(1), 10D506 (2012).
[2]P. E. Stott, "Diagnostics for contemporary fusion experiments," Nucl. Fusion **32**(1), 167 (1992).
[3]N. C. Luhmann, "Instrumentation for magnetically confined fusion plasma diagnostics," Rev. Sci. Instrum. **55**, 279 (1984).
[4]J. T. Slough, A. L. Hoffman, R. D. Milroy, R. Maqueda, and L. C. Steinhauer, "Transport, energy balance and stability of a large-s field-reversed configuration," Phys. Plasmas **2**(6), 2286 (1994).

[5]L. C. Steinhauer, "Review of field-reversed configurations," Phys. Plasmas **18**, 070501 (2011).
[6]M. Y. Wang and G. H. Miley, "Particle orbits in field-reversed mirrors," Nucl. Fusion **19**(1), 39 (1979).
[7]A. S. Landsman, S. A. Cohen, and A. H. Glasser, "Regular and stochastic orbits in a highly prolate field-reversed configuration," Phys. Plasmas **11**(3), 947 (2004).
[8]A. H. Glasser and S. A. Cohen, "Ion and electron acceleration in the field-reversed configuration with an odd-parity rotating magnetic field," Phys. Plasmas **9**(5), 2093–2102 (2002).
[9]T. W. Speiser, "Particle trajectories in model current sheets," J. Geophys. Res. **70**(17), 4219, https://doi.org/10.1029/JZ070i017p04219 (1965).
[10]S. A. Cohen and A. H. Glasser, "Ion heating in the field-reversed configuration by rotating magnetic fields near the ion cyclotron resonance," Phys. Rev. Lett. **85**(24), 5114–5117 (2000).
[11]A. L. Hoffman, H. Y. Guo, K. E. Miller, and R. D. Milroy, "Principal physics of rotating magnetic field current drive of field-reversed configurations," Phys. Plasmas **13**(6), 012507 (2019).
[12]C. Swanson and S. A. Cohen, "The effect of rigid electron rotation on the Grad–Shafranov equilibria of a class of FRC devices," Nucl. Fusion **61**, 086023 (2021).
[13]D. R. Welch, S. A. Cohen, T. C. Genoni, and A. H. Glasser, "Formation of field-reversed configuration plasmas with punctuated-betatron-orbit electrons," Phys. Rev. Lett. **105**, 015002 (2018).
[14]L. C. Steinhauer, "Hybrid equilibria for field-reversed configurations," Phys. Plasmas **18**, 112509 (2011).
[15]E. V. Belova, R. C. Davidson, H. Ji, and M. Yamada, "Kinetic effects on the stability properties of field-reversed configurations. II. Nonlinear evolution," Phys. Plasmas **11**(5), 2523 (2004).
[16]R. D. Milroy, C. C. Kim, and C. R. Sovinec, "Extended magnetohydrodynamic simulations of field reversed configuration formation and sustainment with rotating magnetic field current drive," Phys. Plasmas **17**, 016502 (2010).
[17]R. M. Magee, A. Necas, R. Clary, S. Korepanov, S. Nicks, T. Roche, M. C. Thompson, M. W. Binderbauer, and T. Tajima, "Direct observation of ion acceleration from a beam-driven wave in a magnetic fusion experiment," Nat. Phys. **15**, 281 (2019).
[18]A. Dogariu, S. P. Evans, E. Vinoth, and S. A. Cohen, "Non-invasive neutral atom density measurements using fs-TALIF in a magnetic linear plasma device," in *Proceedings CLEO: Science and Innovations* (Optical Society of America, 2021).
[19]See https://dataspace.princeton.edu/handle/88435/dsp01x920g025r.